

Development of an EUV (13.5nm) Light Source Employing a Dense Plasma Focus in Lithium Vapor

William Partlo^a, Igor Fomenkov^a, Roger Oliver^a, Daniel Birx^b

^aCymer Inc., 16750 Via Del Campo Crt., San Diego, CA 92127

^bApplied Pulse Power Technologies Inc., 3300 Crismore Lane, Oakley, CA 94561

ABSTRACT

Initial characterization efforts of Dense Plasma Focus (DPF) technology showed that efficient conversion of electrical energy into in-band emitted radiation could be achieved. Results previously reported showed that 25J of electrical energy can be converted into 0.38J of in-band, 13.5nm radiation emitted into 2π steradians. This prototype configuration demonstrated a 1.5% conversion efficiency into 2π steradians, but exhibited several major drawbacks. The two greatest issues were excessively high stored energy per pulse and poor stability of the plasma size and position. Such high input energies would limit the maximum pulse repetition rate and poor plasma stability would lead to excessive electrode erosion and large integrated source size.

Recent efforts have concentrated on reducing the required input energy while simultaneously improving stability. The result of these efforts is a DPF system that exhibits stable operation with as little as 1.5J of input energy and has demonstrated pulse repetition rates as high as 2500Hz.

Once a stable, low input energy DPF was achieved, this prototype DPF device was fitted with a simple Lithium vapor delivery system. Pinhole camera images of the Lithium vapor source show that it is stable with a size of less than $350\mu\text{m}$ FWHM. In this technology's present state, the potential in-band collectable EUV optical power is estimated to be 6.9W.

Keywords: EUV Lithography, Dense Plasma Focus, Solid State Pulse Power, Lithium Emission

1. INTRODUCTION

A Dense Plasma Focus (DPF) device has been investigated as a source for EUV lithography because of its potential for high source brightness and high repetition rate operation. A prototype DPF has been constructed that employs an all-solid-state pulse power drive system. This prototype DPF is based on the development work done toward an efficient electric plasma thruster for space applications¹⁻³.

Initial characterization efforts concentrated on demonstrating that this technology could create plasma temperatures sufficiently high for efficient emission of EUV radiation. An in-band conversion efficiency of 1.5% into 2π steradians was demonstrated with the initial prototype. Though a satisfactory conversion efficiency was demonstrated with the initial prototype, several drawbacks were apparent. The input energy of 25J is considered too large for practical scaling to the high repetition rates required for scanning EUV microlithography systems. Additionally, the positional stability exhibited by this initial prototype was poor, leading to a large integrated source size and excessive electrode erosion.

Development efforts since have concentrated on reducing the required input energy while improving the positional stability. Second generation prototypes have been constructed that exhibit stable operation with as little as 1.5J of input energy. The enhanced metrology capabilities of EUV imaging and visible intensified gated camera imaging have helped to diagnose the root causes of pulse-to-pulse instabilities.

Also critical to the success of this EUV source concept is the use of a collection optic tolerant to the presence of Lithium vapor. To achieve maximum in-band emission efficiency, the DPF source will contain Lithium vapor. Lithium has a strong, narrow emission line at 13.5nm from its doubly ionized state. A multi-layer mirror fabricated from Mo/Si layers is not

expected to survive long in the presence of Lithium vapor, so a grazing incidence collector design has been chosen for the primary collection optic. The prototype of this grazing incidence optic has been fabricated. Testing with visible light shows that imperfections in several of the collector's parabolic surfaces introduce wave front errors sufficient to increase the divergence of a 500 μ m source by a factor of two.

2. DENSE PLASMA FOCUS SYSTEM DESCRIPTION

A DPF device consists of a coaxial electrode set driven to a voltage potential difference that results in the formation of a conductive plasma sheath between the inner and outer electrodes. Previously, typical DPF systems operated in the range of 10-50kV between electrodes resulting in large stored energies in the drive capacitor. Careful design of the drive inductance enables operation of this prototype DPF between 1kV to 2kV.

Fig 1 shows a simplified diagram of the electrical drive circuit. The initial storage capacitor, C_0 , is charged on command by the DC power supply. Once full charge is reached, the IGBTs are triggered into conduction causing resonant transfer of energy from C_0 to C_1 . The initial prototype system possessed a C_1 capacitor of 65 μ F. Modifications of this prototype have resulted in a reduction in C_1 down to 5.4 μ F. Reducing C_1 while maintaining the same drive inductance increases the frequency of the drive circuit by the square root of the capacitance ratios, in this case a factor of 3.4. It has been found that stability and efficiency improve with the speed of the final stage in the drive circuit.

Once peak voltage on C_1 is reached, a set pre-ionization sources (not shown in Fig 1) are energized to initiate avalanche break down in the gas between the inner and outer electrodes. The low inductance of the drive circuit ensures a rapid rise in current flow and the application of nearly all of the C_1 voltage across the electrode set.

Once significant current begins to flow through the plasma sheath, $\mathbf{J} \times \mathbf{B}$ forces accelerate the plasma away from the base of the electrode set and toward the end of the center electrode (anode). The flow of electrons and ions as well as the magnetic field and resulting force vector are shown in Fig 2. Simultaneous with the acceleration of the plasma, the current flowing from C_1 through the series combination of the drive inductance and electrode inductance rises toward a maximum.

Because the current density and thus magnetic field fall off linearly with radius, the force vector applied to the plasma sheath also falls off with radius. This radial variation in the forces applied to the sheath lead to a cone shaped plasma as shown in Fig 3. Once the plasma sheath reaches the end of the anode, the current density vectors and magnetic fields are such that a radially inward directed force is applied the plasma sheath near the end of the anode as shown in Fig 3. It is this action that leads to compression and heating of the plasma in a small column at the center of the anode tip.

In addition to forces compressing the plasma radially inward, there are forces attempting to stretch or elongate the compressed plasma column, also shown in Fig 3. As discussed later in this paper, this elongation of the plasma can cause problems with position stability and increase electrode erosion.

3. SPECTRAL MEASUREMENTS

Since the Mo/Si mirror systems exhibit high reflectivity only over a narrow band of wavelengths, detailed measurements of the emission spectrum from this prototype DPF are needed to quantify the useable radiation. By placing a small amount of Lithium on the tip of the anode, the emission spectrum can be recorded and we can determine if the DPF produces a plasma temperature appropriate for production of EUV radiation. Lithium has been proposed as an emission source for EUV lithography because of its narrow spectrum and intense emission into wavelengths well matched to the reflectance band of Mo/Si mirrors⁴.

Fig 4 shows the measured emission spectrum of the DPF Lithium plasma over a range from 10nm to 24nm. Also shown on this graph is the published reflectivity of a typical Mo/Si mirror. The Lithium emission lines between 10nm and 14nm are due to electronic transitions of doubly ionized Lithium, also referred to as Hydrogen-like Lithium. Verifying the wavelength calibration of the spectrometer is simplified by the fact that the Hydrogen-like Lithium lines are narrow and well known. Using this experimental setup, we can locate six electronic transitions of doubly ionized Lithium as shown in Fig 5. The absence of any strong lines above the 2p-1s transition of doubly ionized Lithium is a particular advantage of Lithium as an

EUV emission source. As the Lithium plasma is heated to high temperatures, there are no effective radiative cooling channels above the 13.5nm line. A substantial portion of the radiated energy will be emitted in the 13.5nm line because it is a highly probable transition and each photon carries much more energy than longer wavelength transitions.

The theoretical quantum efficiency for the 13.5nm line can be calculated by dividing the energy of the 2p-1s transition into the sum of the 2p-1s transition energy and the energy required to form doubly ionized Lithium. The literature states that the energy required to doubly ionize Lithium is 81eV^5 . Thus the theoretical quantum efficiency for 13.5nm emission is 53%.

As shown in Fig 4, the 13.5nm Lithium emission line matches well to the Mo/Si reflectance band. A finer resolution spectral scan centered on 13.5nm is shown in Fig 6 along with the published reflectivity of a Mo/Si mirror. The measured bandwidth for this 13.5nm emission line is 0.03nm. It is thought that this result may be spectrometer resolution limited and the bandwidth of this emission line is likely less than 0.03nm. Fortunately, the exact bandwidth of this emission line is unimportant to the operation of the Mo/Si mirror since even the measured 0.03nm result is much more narrow than the reflectance bandwidth of the Mo/Si mirror.

4. EUV SOURCE SIZE MEASUREMENTS

Once the capability of the DPF to produce high plasma temperatures was verified, efforts were concentrated on improving stability and reducing the required input energy. Since the initial prototype DPF was operated with a background gas of Argon and our Lithium vapor delivery techniques are immature, the following characterization efforts were performed with Argon only. Fortunately, Argon does possess emission lines in the EUV region, though very weak, so EUV pinhole images can be taken of various configurations.

The first step toward a better understanding of the DPF instabilities was to take visible wavelength gated camera images of the plasma formation. Fig 7 shows a time sliced sequence of the DPF formation with a solid anode. Each frame is an average of 10 images taken in 200ns steps. The initial frames show the run down phase with the main DPF forming during the 600ns frame. Following formation of the DPF, the plasma sheath continues to travel axially until it completely detaches from the anode. One can also see visible emission from the anode itself due to excessive heating caused by direct contact with the hottest portion of the plasma.

Switching to a hollow anode easily solves the hot spot formation on the tip of the electrode. The formation of the DPF with a hollow anode is shown in Fig 8. Again the frames are an average of 10 images each taken in 200ns steps. As with the solid anode, the plasma sheath continues its axial travel after formation of the DPF. Though no excessive heating of the anode is observed since there is no solid material near the hottest portions of the plasma, there still remains the problem of unstable operation due to the plasma detaching from the anode. As shown in Fig 8, unstable operation is evidenced by the arc-over events that occur at random locations around the edge of the anode.

The detachment problem was addressed by additional modifications to the electrode configuration. A ceramic component similar in shape to that shown in Fig 9 was placed above the tip of the anode. This component acts as a physical barrier preventing the plasma from accelerating past the tip of the anode and detaching from the anode. Unfortunately, the presence of this "blast shield" prevents side-on viewing of the plasma run-down and compression phases. The geometry is such that one can still view the edges of the anode by looking through the hole in the blast shield at a slight angle. Observations made by eye show that no arc-over events occur when operating within a range of stored energies and buffer gas pressures.

To facilitate EUV imaging of the resulting stable plasma, a pinhole camera arrangement was employed as shown in Fig 10. A $50\mu\text{m}$ pinhole located on axis 25cm from the tip of the anode is used to form an image on a back-side illuminated CCD array located 32cm from the pinhole. Spectral filtering is provided by a $1\mu\text{m}$ thick Beryllium foil placed just behind the pinhole. The published transmission of this foil is shown in Fig 11. The spatial resolution of this pinhole camera is limited by both geometry of the pinhole and diffraction at the pinhole. The resulting convolution of the geometric and diffraction spot sizes is shown in Fig 12 giving a system resolution of $92\mu\text{m}$ under the assumption of 13.5nm illumination.

An EUV source image taken while operating at 10Hz with a buffer gas of Argon is shown in Fig 13. The resulting source size is $313\mu\text{m}$ FWHM. This image was taken with a 90 second exposure while operating continuously at 10Hz, so 900

pulses were integrated on the array to form this image. The resulting small integrated source size demonstrates that the EUV source is both small and highly stable in its location.

The size of the hot plasma indicated by EUV emission can be compared to the dimensions of the hollow anode. Fig 14 shows the measured EUV source size on the same scale as the anode's inner and outer radii.

5. REPETITION RATE SCALING

One promising feature of this DPF device is its proven high repetition rate capability when used as an electric plasma thruster for space applications¹⁻³. As a plasma thruster, short bursts of 3,000Hz operation are routinely demonstrated. To investigate the repetition rate performance of this DPF device as an EUV source, we operated at increasing repetition rates in short bursts while taking EUV pinhole camera images.

Fig 15 shows the measured EUV source profiles for repetition rates from 10Hz to 1000Hz. As the repetition rate is increased up to 1000Hz the source brightness actually increases, that is the source size remains the same or smaller while the total EUV output increases. EUV images were taken up to the DC power supply limit of 2500Hz. The measured source profile for 2500Hz is shown in Fig 16 along with the 1000Hz result for comparison. The integrated source size for 2500Hz is slightly larger than for 1000Hz, but the total emission is higher for 2500Hz.

It is not known for certain the cause of the increase in total EUV emission with increasing repetition rate. One possibility that suggests itself is the presence or absence of contaminants "boiled" off from surfaces during previous pulses. As the period between pulses decreases with higher repetition rate, these contaminants have less time to re-condense. One attribute of this prototype's performance that supports the idea of contaminate interactions is a 30 minute "warm-up" characteristic exhibited by this machine. Even after maintaining vacuum for more than a week and running for greater than 10^6 pulses, the total EUV emission goes through a transient period of approximately 30 minutes upon restart after no running for several hours. This characteristic repeats itself after each extended off period.

This prototype was constructed without any special cleaning or handling procedures and the vacuum pump is a two stage rotary pump used without a fore-line trap. For future machines, much greater attention will be given to material choices, parts handling, and clean vacuum technology.

6. LITHIUM VAPOR EMISSION IMAGES

Once a sufficiently stable, low energy DPF had been demonstrated, efforts turned toward generating Lithium vapor in the region near the tip of the anode and characterizing the source dimensions and absolute in-band emission. Two concepts for providing Lithium vapor were implemented. Both concepts attempt to address the problem of boiling Lithium and the sporadic delivery of Lithium vapor that results.

The first concept, shown in Fig 17, was to insert a rod of porous Tungsten into the center of the anode. This Tungsten plug was placed deep inside that anode such that the hot dense plasma produced by the DPF did not come into contact with the Tungsten. The porous Tungsten was then saturated with Lithium by filling the anode/Tungsten plug assembly with Lithium pellets and heating the assembly in a vacuum oven. Once the porous Tungsten was filled with Lithium, the assembly was cooled and installed in the prototype DPF. The strategy then was to operate the DPF at a moderate repetition rate sufficient to heat the anode assembly above the melting point of Lithium and produce a partial pressure of Lithium vapor. We had no method for measuring the anode assembly temperature and can only estimate that it was no higher than approximately 600°C. According to the literature, a temperature of 600°C leads to a Lithium vapor pressure of only 63mT.

The second concept, also shown in Fig 17, was to insert powdered Lithium Hydride, LiH, down inside the hollow anode. By raising the temperature of the anode during operation, the LiH decomposes releasing Lithium vapor. As with the porous Tungsten concept, the level of LiH powder was adjusted so that the hot dense plasma of the DPF never contacted the LiH.

In both concepts, a slow flow of Argon is sent up the center of the anode to act as a carrier gas to aid in transporting the Lithium vapor up to the tip of the anode. The porous Tungsten concept had an advantage in that we could machine small grooves on the outer diameter of the porous Tungsten plug to allow unrestricted flow of Argon from the bottom of the anode,

around the porous Tungsten, and up to the tip of the anode. The LiH concept, in this initial implementation, at times would block the flow of Argon causing a build up of Argon back pressure and the eventual ejection of the LiH powder from within the center of the anode. Once the LiH is ejected, the machine must be disassembled and cleaned of all stray LiH powder.

The resulting pinhole camera images for both Lithium vapor concepts are shown in Fig 18. The LiH concept exhibited slightly more emission and a larger source size, but these initial experiments are too crude to say if the difference was due to the Lithium delivery method. Also shown in Fig 18 is the measured EUV pinhole image with just the Argon carrier gas flowing up the center of the anode. This Argon image was taken in two ways. The first was to operate the DPF at a low enough repetition rate such that the temperature of all components was below the melting point of Lithium and thus no significant Lithium vapor pressure exists. The second method was to run the DPF at a repetition rate such that the anode assembly reached temperatures sufficient to vaporize Lithium and then maintain operation until all available Lithium was vaporized. The second method is preferred since it allows us to take Argon images with all conditions the same as with Lithium vapor, including repetition rate. As the curves in Fig 20 show, virtually all of the measured EUV emission is generated by the Lithium vapor.

It is believed that higher levels of 13.5nm output can be achieved if the partial pressure of Lithium vapor were increased beyond the levels produced in these experiments. The anecdotal evidence for this belief is the much higher level of output occasionally measured during our first attempts at producing Lithium vapor by simply putting Lithium pellets at the bottom of the hollow anode. When the pool of liquid Lithium boiled or bubbled, large increases in 13.5nm emission were observed.

7. ESTIMATED IN-BAND COLLECTABLE OPTICAL POWER

Using the porous Tungsten Lithium vapor delivery concept, we measured the absolute in-band emission using a coated IRD photodiode. The measured waveshapes for both the V_{C1} waveshape and the diode output are shown in Fig 19. The diode was terminated into 50Ω but its self capacitance is large enough to cause the long exponential tail shown in the figure. The sharp rising edge of the diode signal marks the collapse and compression of the plasma and the onset of EUV production. This event is nearly coincident with the zero crossing of the V_{C1} waveshape. Substantially all of the electrical energy left in the circuit at this point is inductively stored. The length of the run-down phase, the size of the $C1$ capacitance, and the pressure of the buffer gas are all optimized to create this condition in an attempt to maximize the peak current flowing through the compressed plasma.

The 400V overshoot of the V_{C1} waveshape represents 7.6% of the energy initially stored on $C1$, or 0.42J. The present circuit design does not capture and recover this energy in a manner similar to the pulse power circuit design used to drive Cymer's excimer lasers. This capability can be added with only moderate effort and should improve electrode lifetime since this energy is deposited into the electrode region during a period when the plasma column has disintegrated into a random, non-uniform shape.

The area under the IRD photodiode curve shown in Fig 19 divided by 50Ω gives the charge created by the 13.5nm photons incident on the photodiode. By accounting for the quantum efficiency of the photodiode, the transmission of the diode filter, the steradians subtended by the diode, and the transmission of the buffer gas, we can convert the diode waveshape into a value for the total in-band emission into 2π steradians. The resulting in-band emission is 12.9mj into 2π steradians giving an in-band emission efficiency of 0.23%.

To estimate the potential total in-band optical power produced by this configuration, we assume that the repetition rate will be limited by thermal considerations at 25kW of input power. With this assumption and a 5.6J per pulse input energy this system can reach 4.4kHz operation. An emission efficiency of 0.23% results in 57.5W of in-band optical power emitted into 2π steradians.

Not all of this 57.5W of emitted in-band power is available for collection for three reasons. The first is that the presence of the ceramic blast shield prevents collection of ray angles too far off axis. The second reason for a limited collection angle is the source size. Collecting all 2π steradians of this source would produce a source etendue greater than that of the lithography tool. The third limitation on collection angle is due to the limits on the collection optic itself. The first generation grazing incidence collector proposed for this source and described in the next section has a 6% of 2π steradians collection efficiency and the second generation collector currently under development will have a 12% collection efficiency.

Accounting for the 12% collection efficiency of the second generation optic leads to an in-band, collectable optical power of 6.9W

8. GRAZING INCIDENCE COLLECTOR

As important as creating an EUV source with high spectral brightness is collecting and relaying this radiation to a region safe for use with the sensitive Mo/Si EUV mirrors. Since this DPF source will use Lithium vapor as its emission specie, some background level of Lithium vapor is expected to be near the primary collection optic. Mo/Si multi-layer EUV mirrors are expected to degrade under exposure to Lithium vapor so an alternate collection optic is required. Use of a collector based on grazing incidence reflections offers promise because such an optic exhibits high reflectivity and can be fabricated from materials inert to Lithium vapor exposure.

The multiple shells of the prototype grazing incidence collector were fabricated with electroplated Nickel coated with Palladium. Fig 20 shows the published reflectivity versus angle for various candidate coating materials. From these curves one can see that Molybdenum exhibits superior reflectivity up to 20° grazing incidence. In fact, if a grazing incidence collector were fabricated using a Molybdenum coating with grazing incidence angles no greater than 20° it would have higher efficiency than a multi-layer EUV mirror with equivalent collection angle.

Palladium was chosen as the coating material for this prototype because the vendor, Parallax Research Inc., had extensive experience with Palladium coatings. Because of the reduced reflectivity of Palladium at higher grazing incidence angles, the design criteria for this optic was for a single reflection and grazing incidence angle no greater than 10°. A summary of the design criteria is given in the following table:

Collector Output:	Collimated Beam
Output Beam Diameter:	50mm
Distance to Entrance:	45mm
Number of Shells:	5
Grazing Angle:	<10°
Collector Length:	65mm
Reflecting Coating:	Palladium
Collection Angle:	40°
Solid Angle:	0.38 Sterad (0.34NA)

While this prototype optic operates at an impressive sounding 0.34NA, it collects only 6% of the available 2π solid angle. A CAD rendering of this optic is shown in Fig 24. The cut away view shows the five nested shells.

Visible light testing of this optic was performed both in the far field and near field. The optical setups for these tests are shown in Fig 21. The output from a 50 μ m diameter fiber was used to simulate point source illumination with an illumination angle sufficient to fill the full collection angle of the optic under test. For far field measurements, a conventional lens with $f=300$ mm was used to focus the collimated output from the test optic onto a CCD array placed at the focal plane of the $f=300$ mm lens. For the near field measurements, an aperture was placed at the focal plane of the $f=300$ mm lens and the camera and lens were positioned to form an image of the collector's exit aperture on the CCD array.

The measured far field pattern for this prototype optic is shown in Fig 22. The upper left corner intensity plot shows the performance of the entire optic with a FWHM divergence of 1.8mrad and a FW90% divergence of 5.0mrad. The remaining five intensity plots show the far field pattern created by each of the five individual shells (Refl. 1 being the outer most shell and Refl. 5 the inner most). These measurements show that the outer most shell exhibits worse performance than the inner shells.

The measured near field performance is shown in Fig 23. The lower left intensity plot shows the illumination at the exit of the collector with no aperturing at the focal plain of the $f=300$ lens. The shadowing from the support spokes and the finite thickness of the shells can be seen. The remaining three intensity plots were recorded with an aperture placed at the focal plane of the $f=300$ mm lens. The aperture is made smaller from left to right (10mrad down to 3.3mrad). As the aperture size

is reduced, and thus higher divergence angles rejected, the near field pattern becomes dim in the regions where the shells deviate from their desired shape. The outer most shell shows the worst wave front errors and the second most outer shell also shows some imperfections.

Since this optic will be used to collect light from a small but extended source, we tested its performance when illuminated by a 500 μ m diameter fiber bundle. The resulting far field divergence is shown in Fig 25 along with the simulated divergence from this source size assuming a perfect optic of this type. This prototype optic increases the theoretical divergence by a factor of two.

It has been shown that the wavefront error produced by the outer two shells is due to deformation under their own weight. The individual shells are fabricated by electroplating Nickel onto a polished mandrel. The thickness of the electroplated Nickel was chosen for ease of fabrication and release from the mandrel. Thicker shells have since been electroplated, successfully released from the mandrel, and are currently undergoing optical testing.

9. CONCLUSIONS

Initial investigations of a stable DPF configuration show that there are no obvious gas dynamics issues with regard to repetition rate operation up to 2500Hz. Near term efforts will be made to investigate repetition rates up to and beyond those anticipated for a production EUV source.

Emission from a Lithium vapor plasma has been found to be efficient with the hopeful prospect of higher efficiency with increases in the available partial pressure of Lithium vapor.

The first generation of grazing incidence collector, though imperfect, shows promise for a rugged, low cost method of re-imaging the DPF source to a region suitable for use with Mo/Si multilayer mirrors. A second generation design, with twice the collection efficiency, has been initiated with improvements suggested from test results of the first generation prototype.

Currently the greatest unknown of importance is the electrode and collector lifetime. Significant progress has been made in the past year to the point where 10^6 pulse runs show no obvious wear. A dedicated life test will be initiated in the near term to better quantify the expected life time of these two critical components.

10. ACKNOWLEDGMENTS

The authors have made extensive use of the EUV transmission data made available by Lawrence Berkeley Labs on their web sight: http://www-cxro.lbl.gov/optical_constants/ and would like to thank those responsible.

11. REFERENCES

1. J. Ziemer, E. Cubbin, E. Choueiri, and D. Bix, "Performance Characterization of a High Efficiency Gas-Fed Pulsed Plasma Thruster," *33rd AIAA/ASME/SAE/ASEE Joint Propulsion Conference*, Seattle, WA, 1997.
2. J. Ziemer, E. Choueiri, and D. Bix, "Trends in Performance Improvements of a Gas-Fed Pulsed Plasma Thruster," *25th International Electric Propulsion Conference*, Cleveland, OH, 1997.
3. D. Bix, "Plasma Gun and Methods for the use Thereof," *US Patent 5,866,871*, Feb. 2, 1999.
4. M. Klosner and W. Silfvast, "Feasibility of Various Discharge Configurations for High Intensity Lithium Vapor Discharge Source at 13.5nm for EUVL," *OSA TOPS on Extreme Ultraviolet Lithograph*, Vol. 4, May, 1996.
5. W. Silfvast, "Efficient Narrow Spectral Width Soft-X-Ray Discharge Sources," *US Patent 5,499,282*, Mar., 1996.

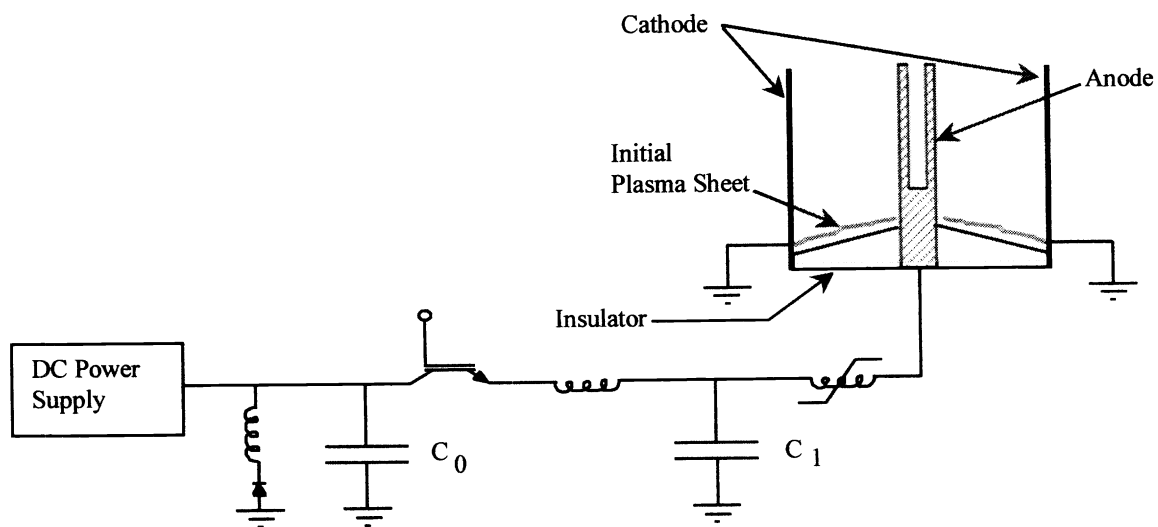


Fig 1. Simplified diagram of the electrical drive circuit.

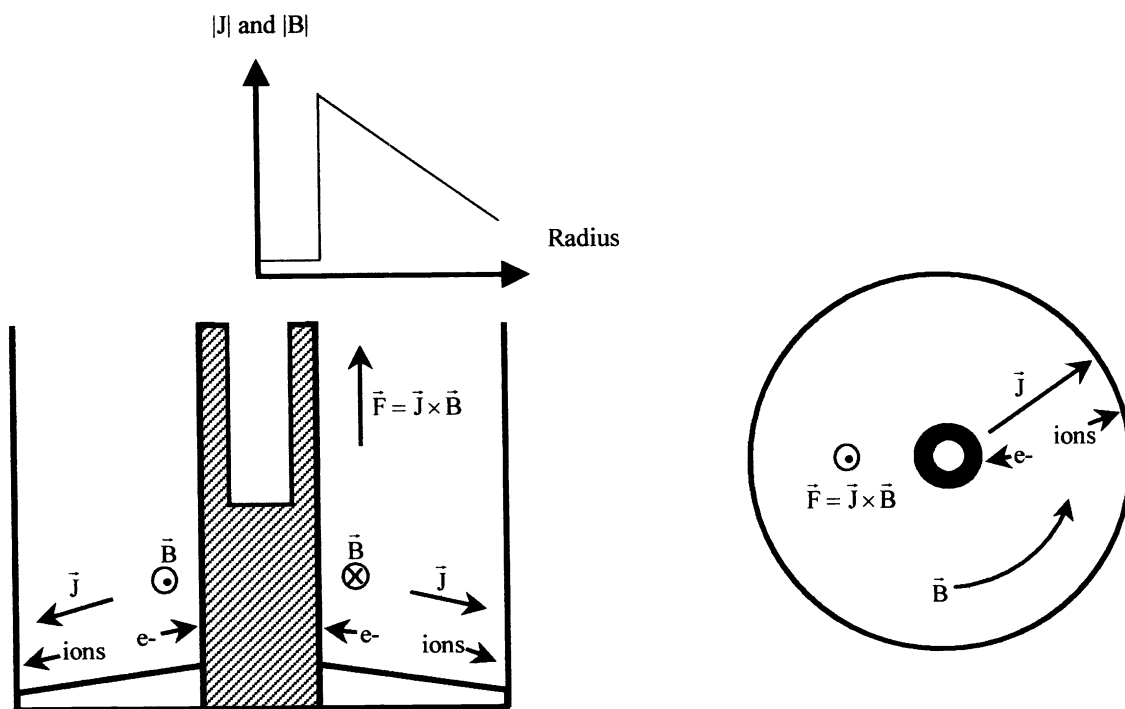


Fig 2. Diagram showing the flow of electrons and ions as well as the magnetic field and resulting force vector.

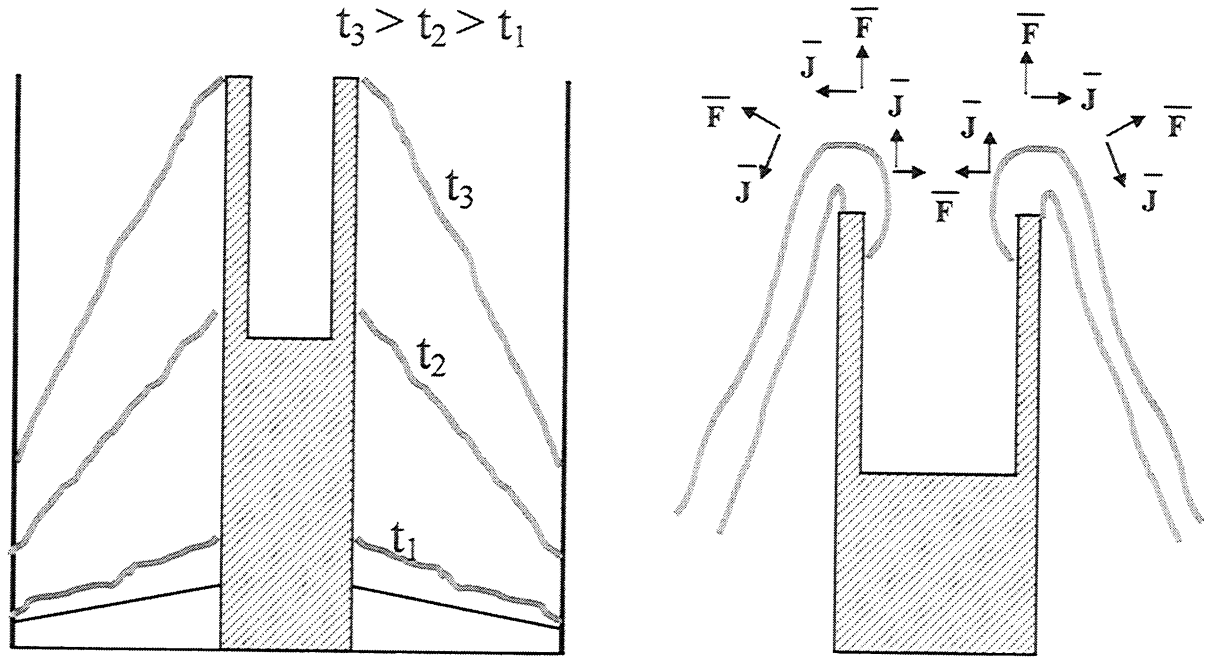


Fig 3. The radial variation in the forces applied lead to a cone shaped plasma sheath (left figure). Once the plasma reaches the end of the anode, inward directed forces compress the plasma (right figure).

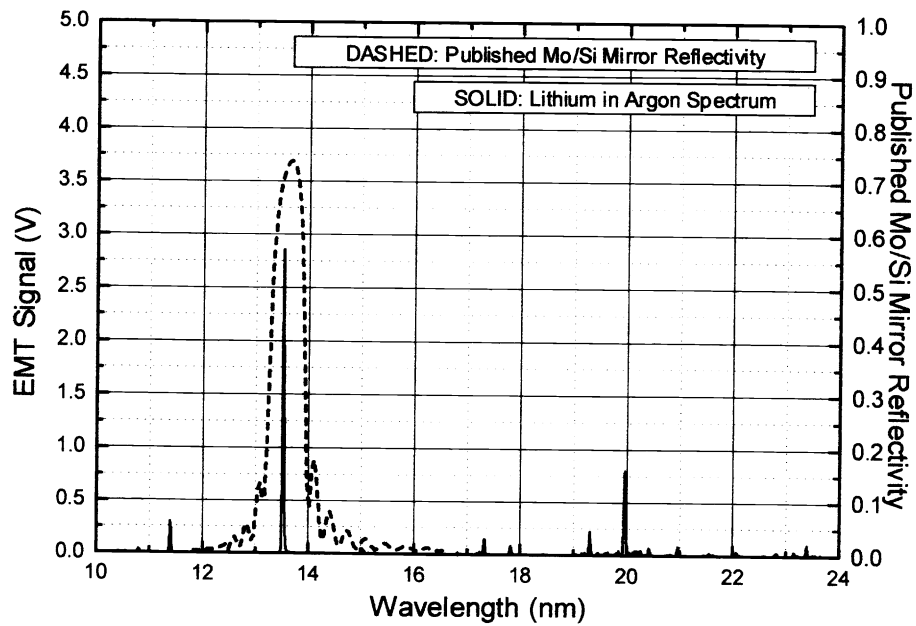


Fig 4. Measured emission spectrum of the DPF Lithium plasma over a range from 10nm to 24nm. Also shown is the published reflectivity of a Mo/Si mirror.

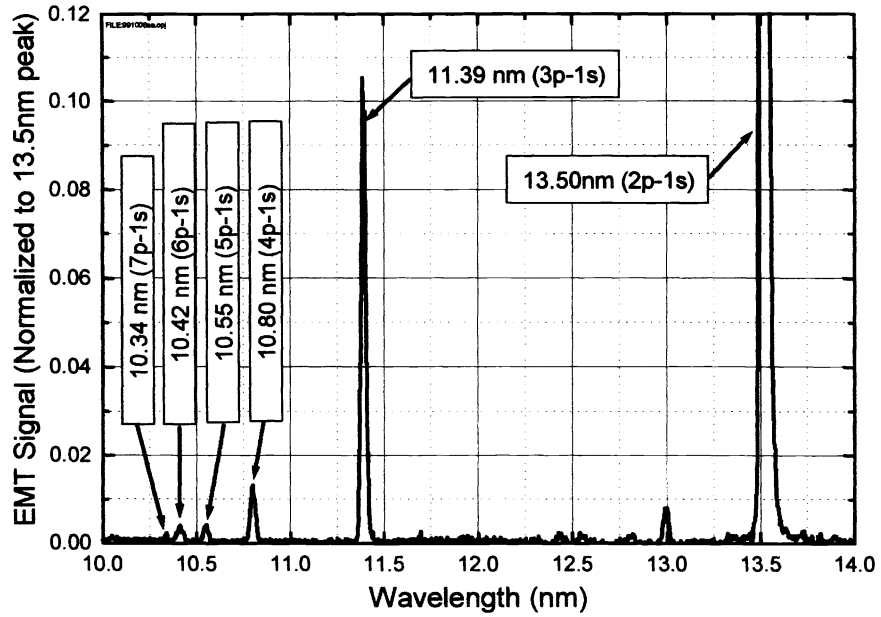


Fig 5. A spectral scan from 10nm to 14nm shows the emission from 6 electronic states of doubly ionized Lithium

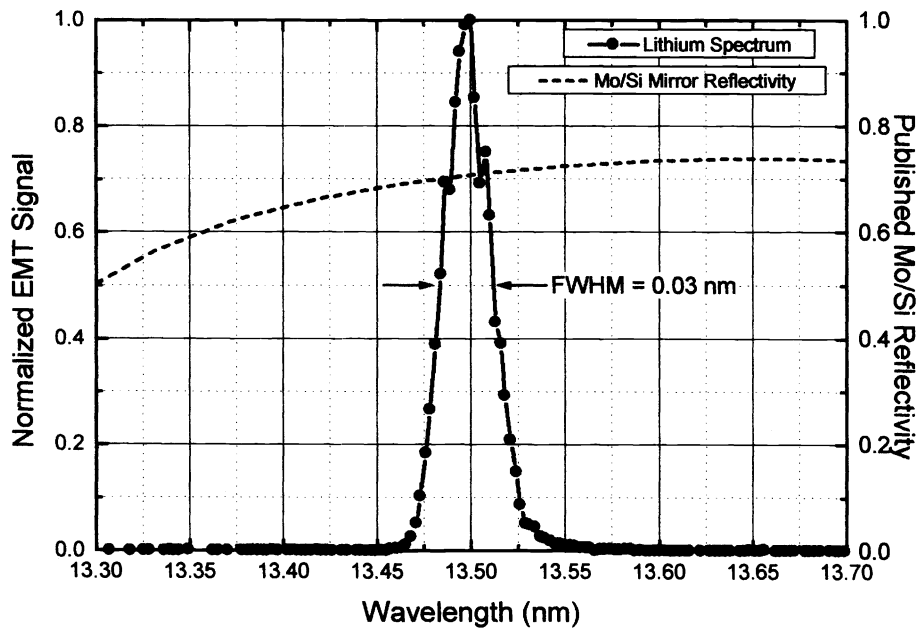


Fig 6. A spectral scan centered on 13.5nm shows a spectrometer-limited bandwidth of 0.03nm.

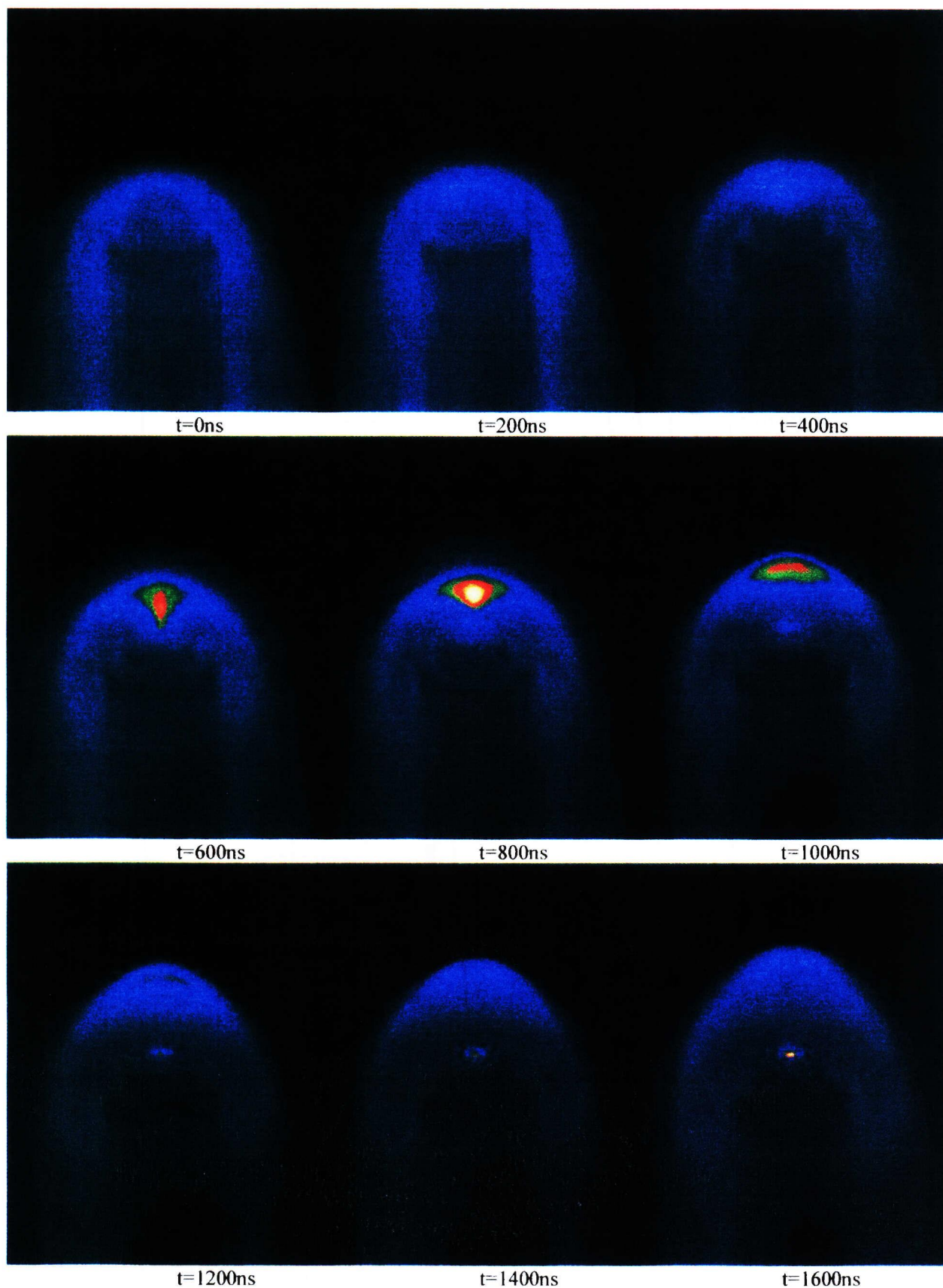


Fig 7. Time sliced sequence of the DPF formation with a solid anode.

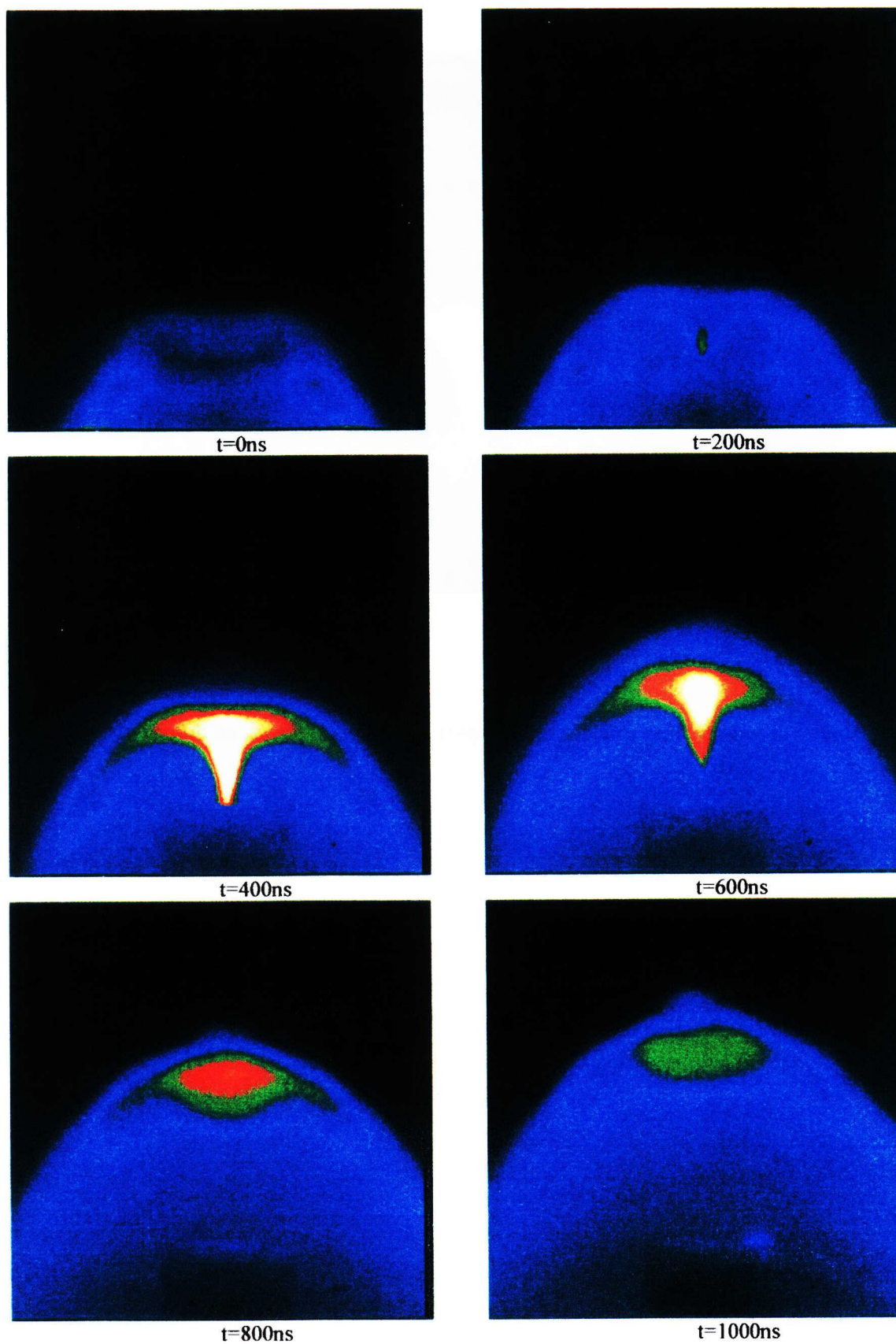


Fig 8. Time sliced sequence of the DPF formation with a hollow anode.

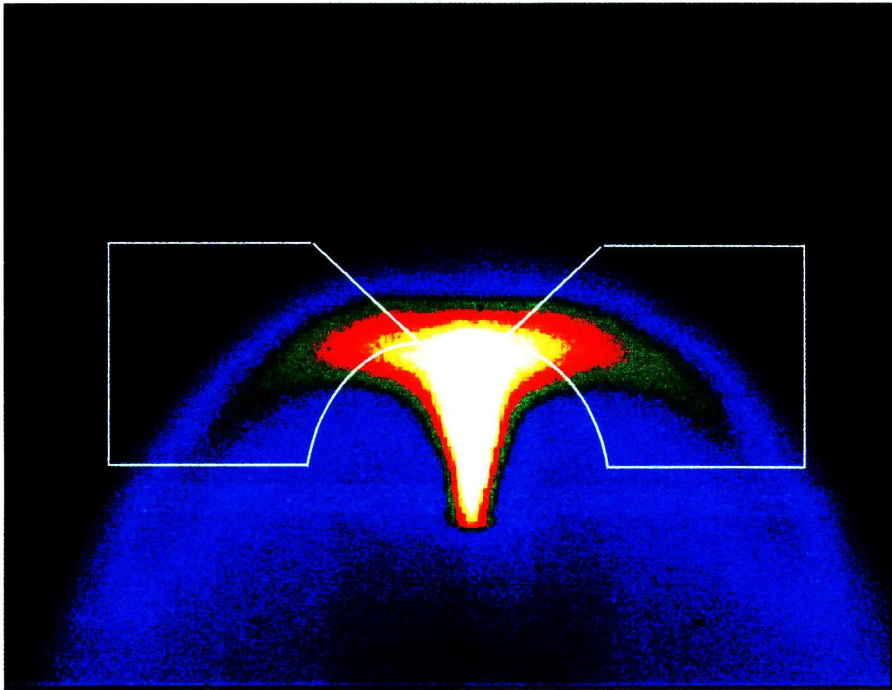


Fig 9. Outline of ceramic "blast shield" used to impede axial travel of plasma off the end of the anode.

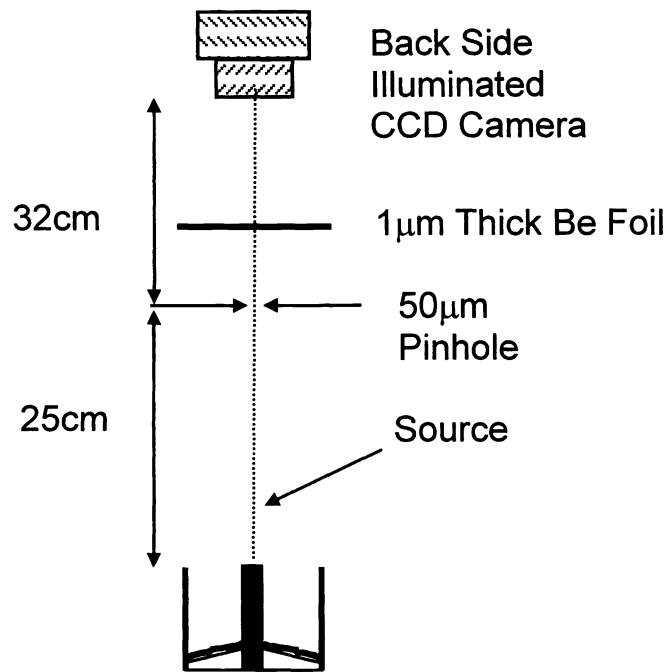


Fig 10. Pin hole camera arrangement used for taking EUV images.

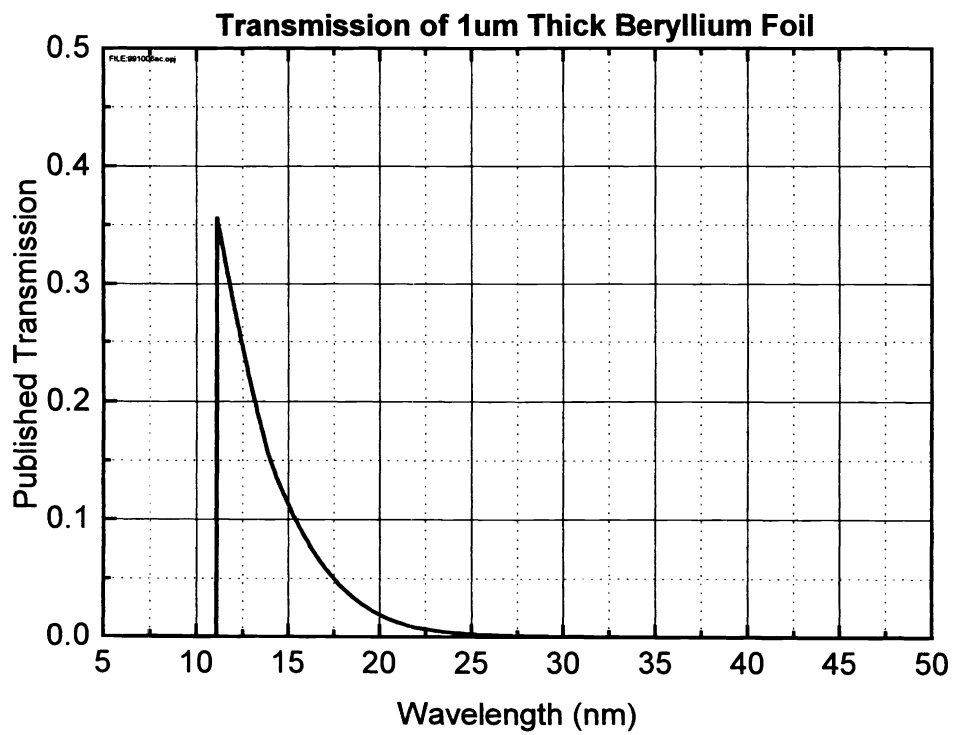


Fig 11. Published EUV transmission of 1µm thick Beryllium foil.

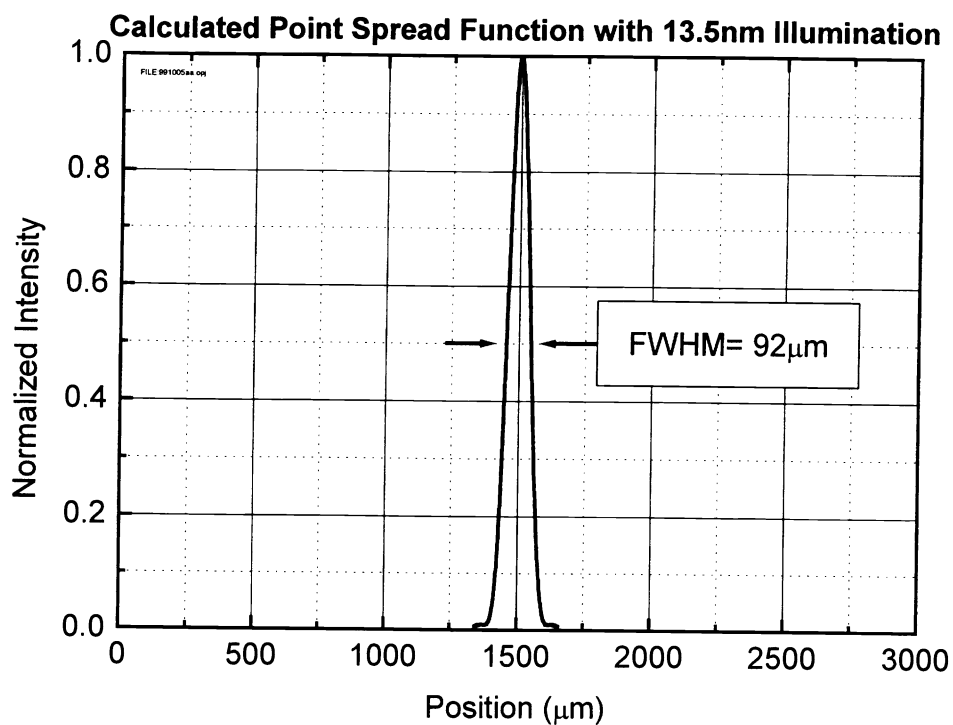


Fig 12. Calculated spatial resolution of pinhole camera.

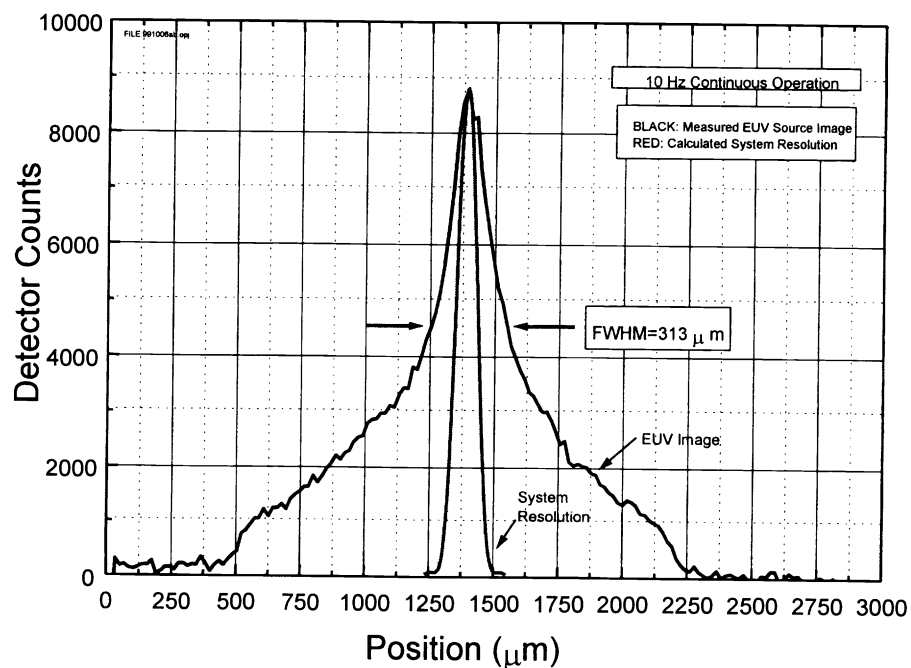


Fig 13. EUV source image taken while operating at 10Hz with an Argon buffer gas.

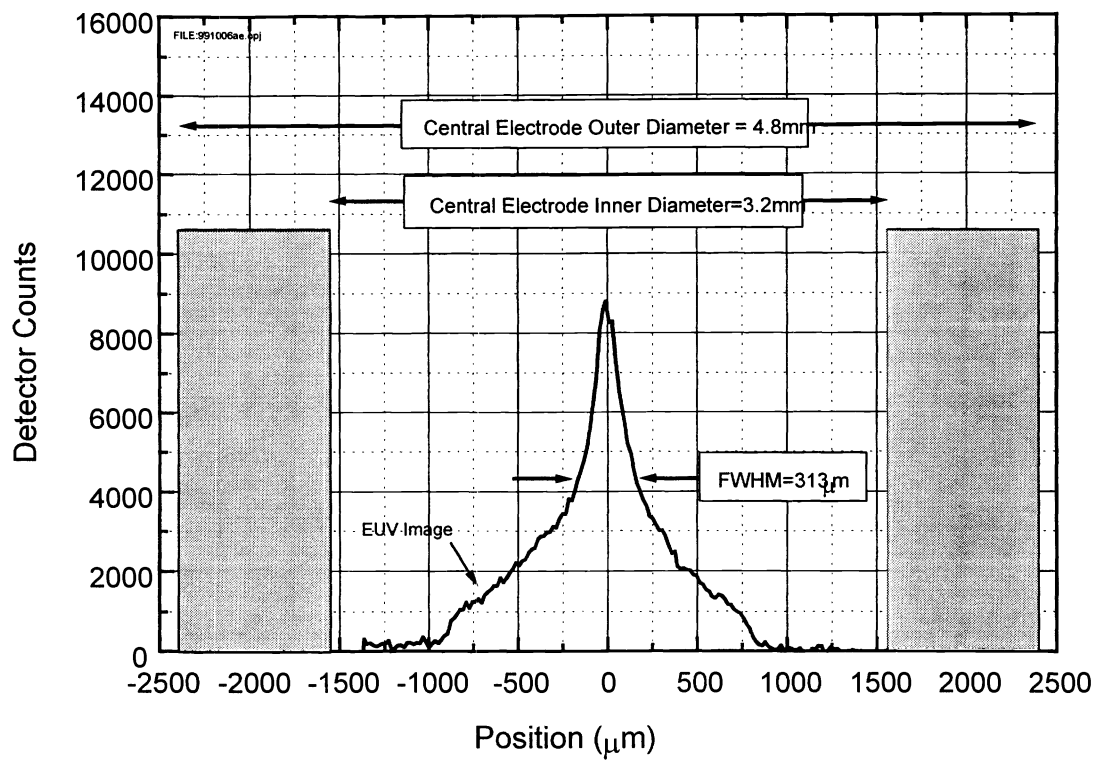


Fig 14. EUV source image plotted relative to the anode dimensions.

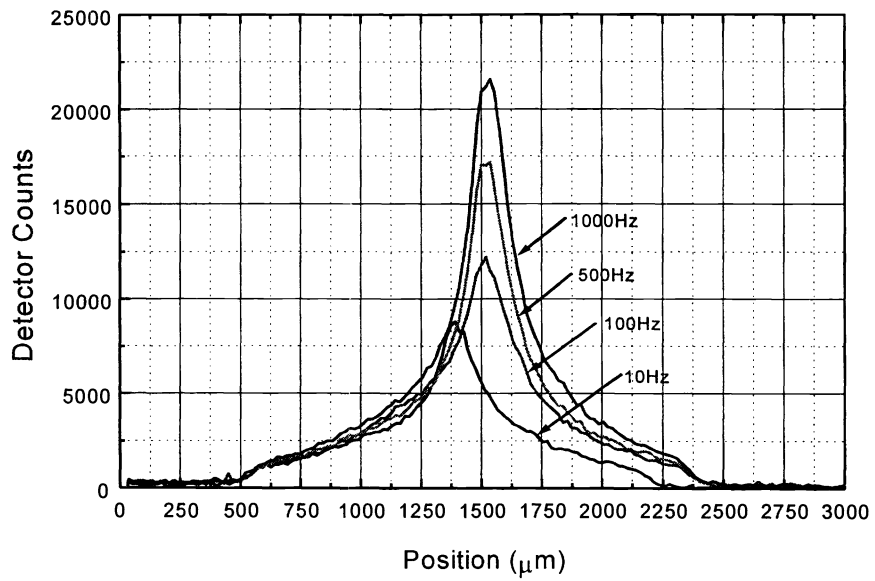


Fig 15. Measured EUV profiles for repetition rates from 10Hz to 1000Hz.

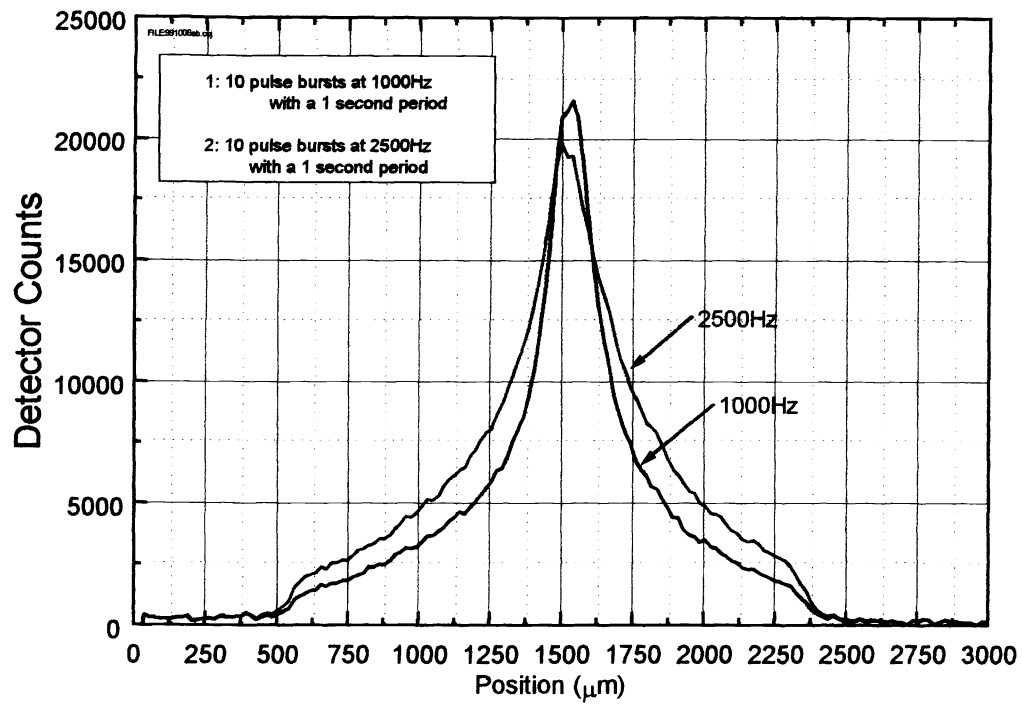


Fig 16. Measured EUV profile for 2500Hz operation with 1000Hz profile for comparison.

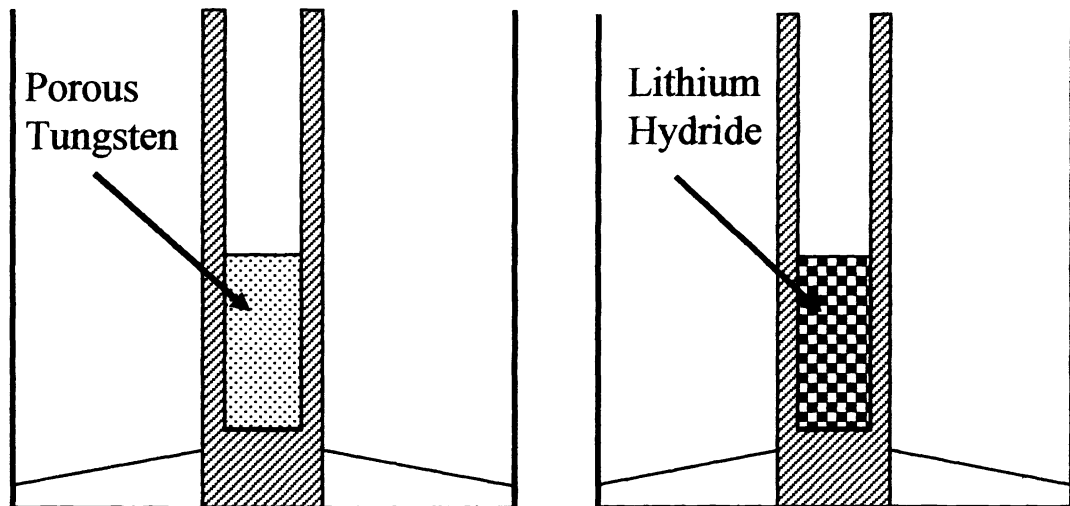


Fig 17. Two concepts of Lithium vapor delivery system.

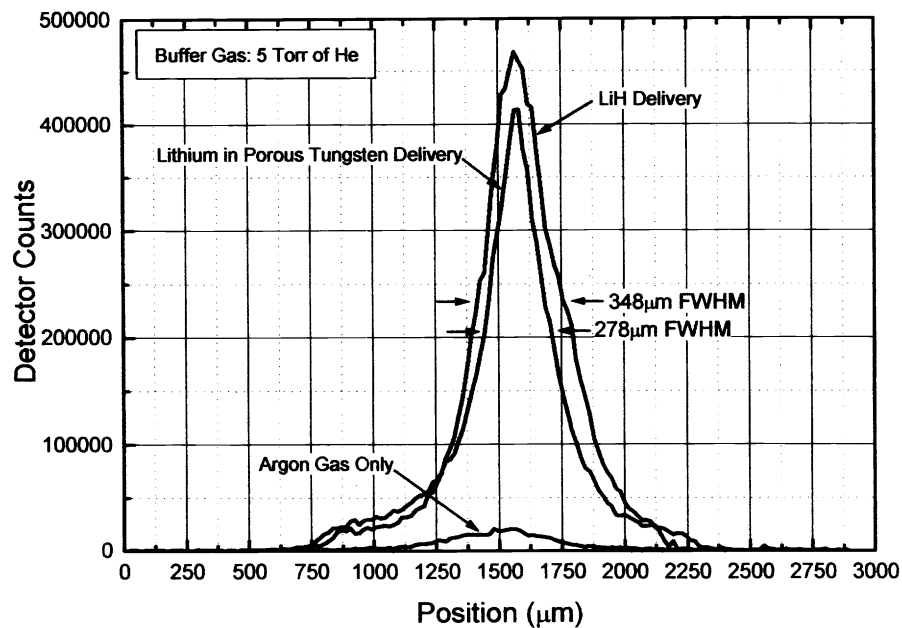


Fig 18. Measured EUV image of Lithium vapor source with two different delivery concepts.

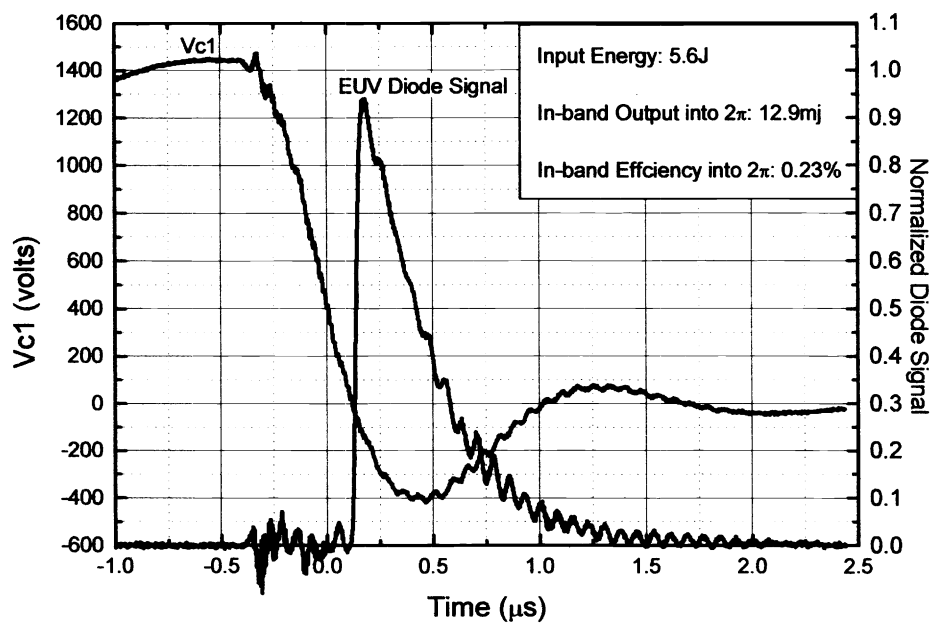


Fig 19. Measured V_{c1} waveshape and EUV photodiode output for Lithium Vapor DPF.

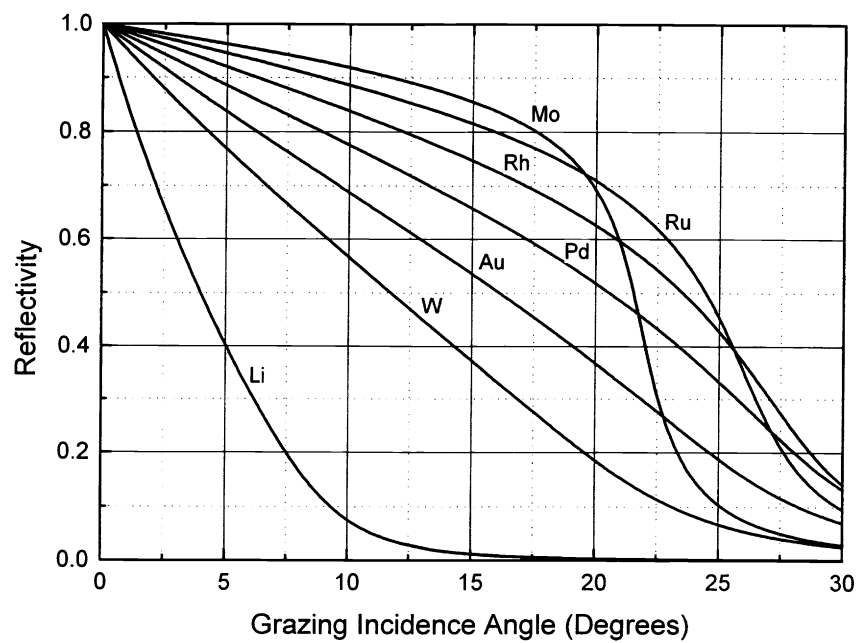


Fig 20. Published 13.5nm reflectivity vs. angle for various candidate grazing incidence plating materials

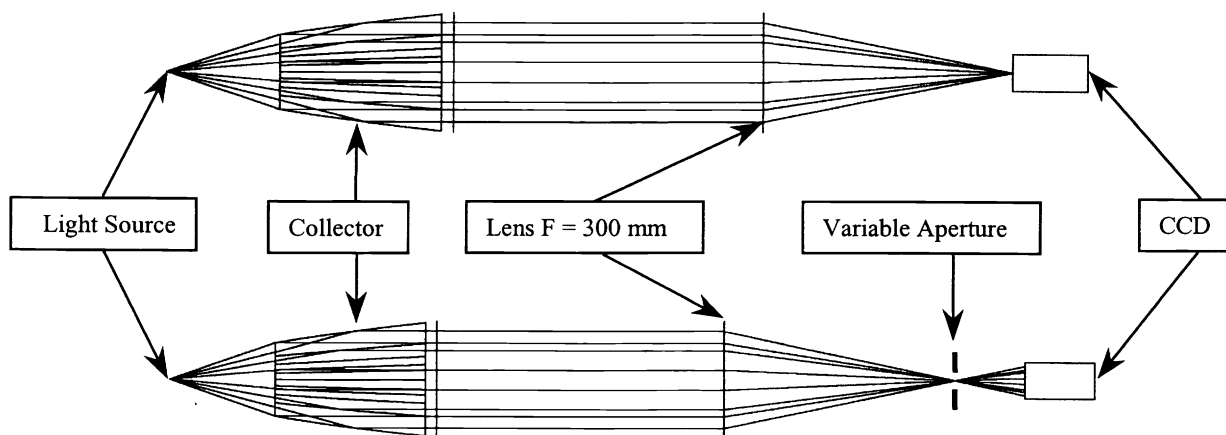


Fig 21. Optical setup used to test prototype grazing incidence collector.

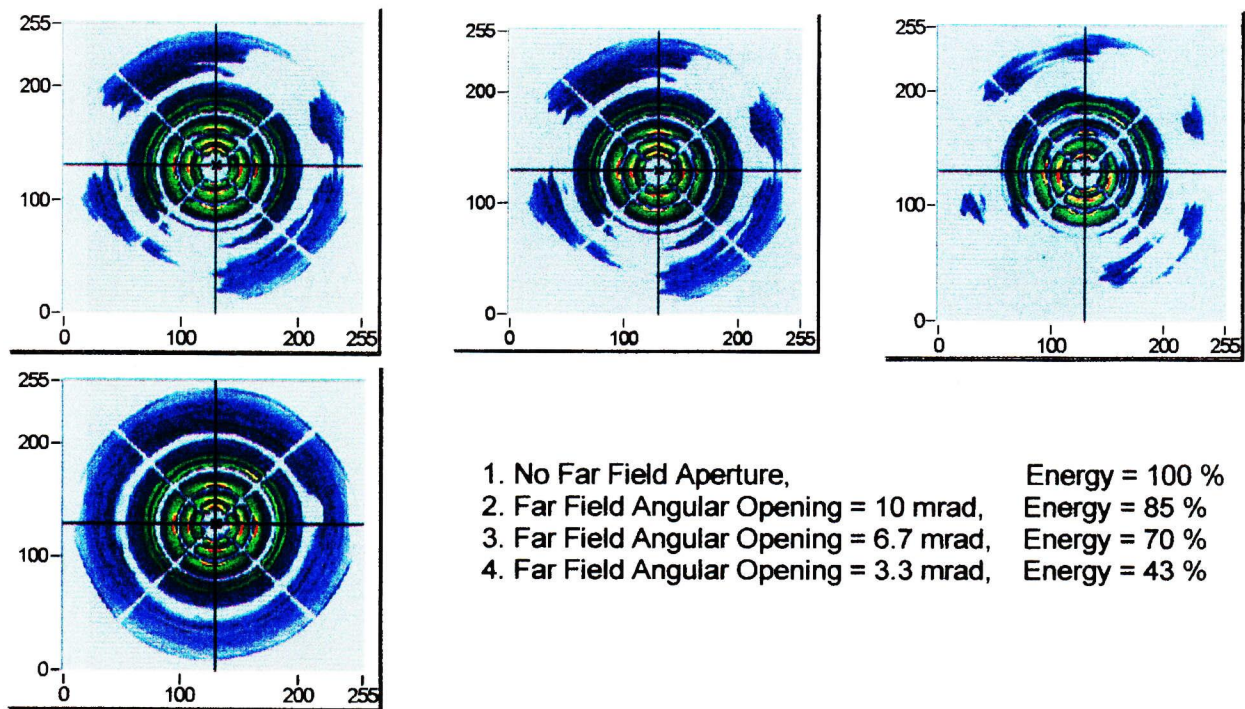
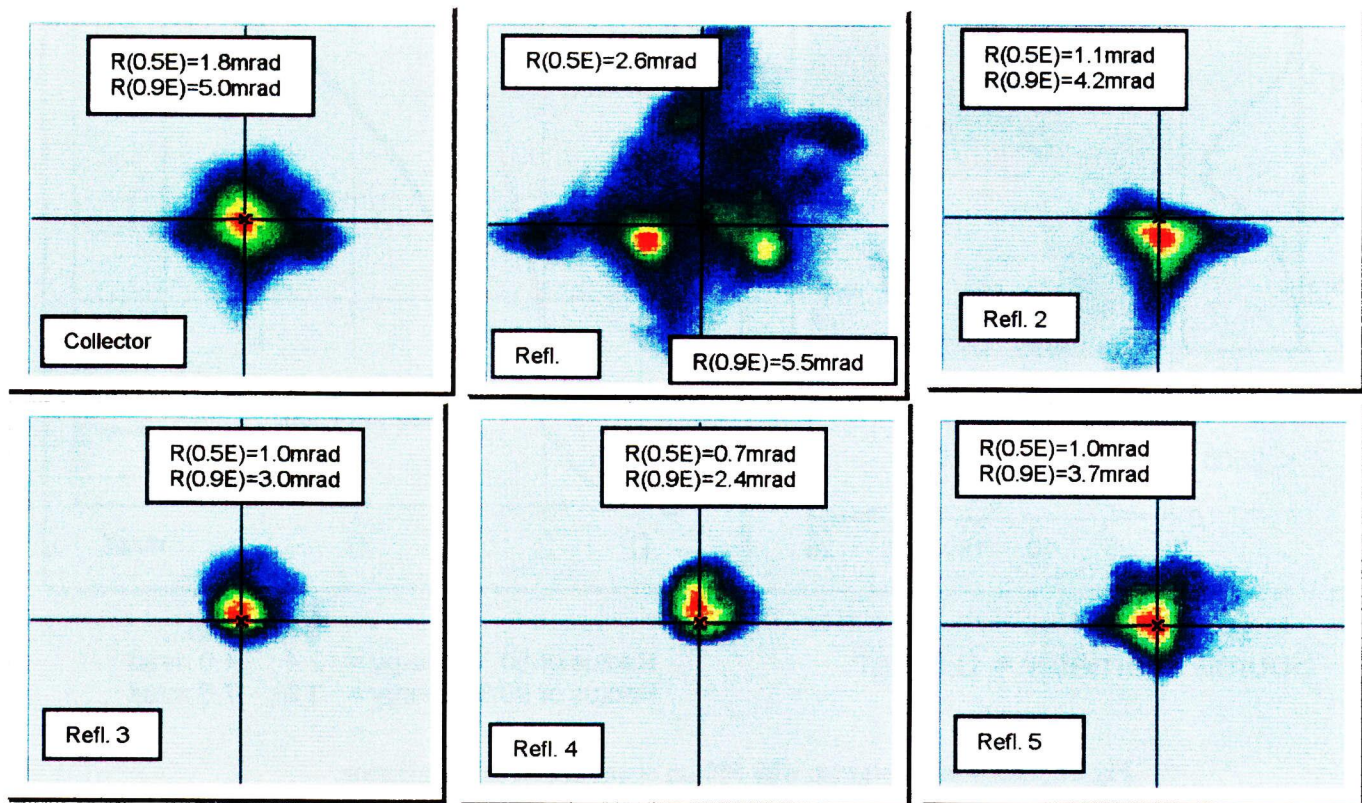
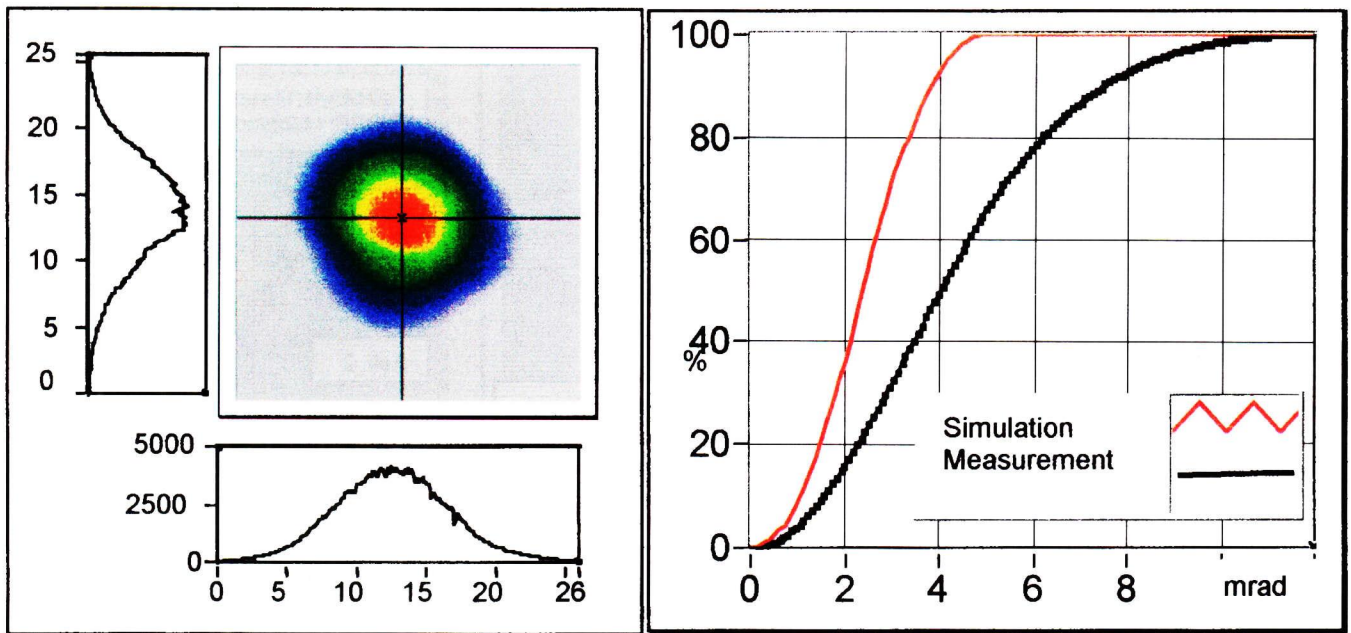


Fig 23. Measured near field performance of prototype grazing incidence collector.



Source Diameter = 0.5mm

	Sim.	Exp.
Radius of 50 % Energy =	2.4 ;	4.0 mrad
Radius of 90 % Energy =	3.9 ;	7.6 mrad

Fig 24. Measured divergence with 500μm diameter source illumination.

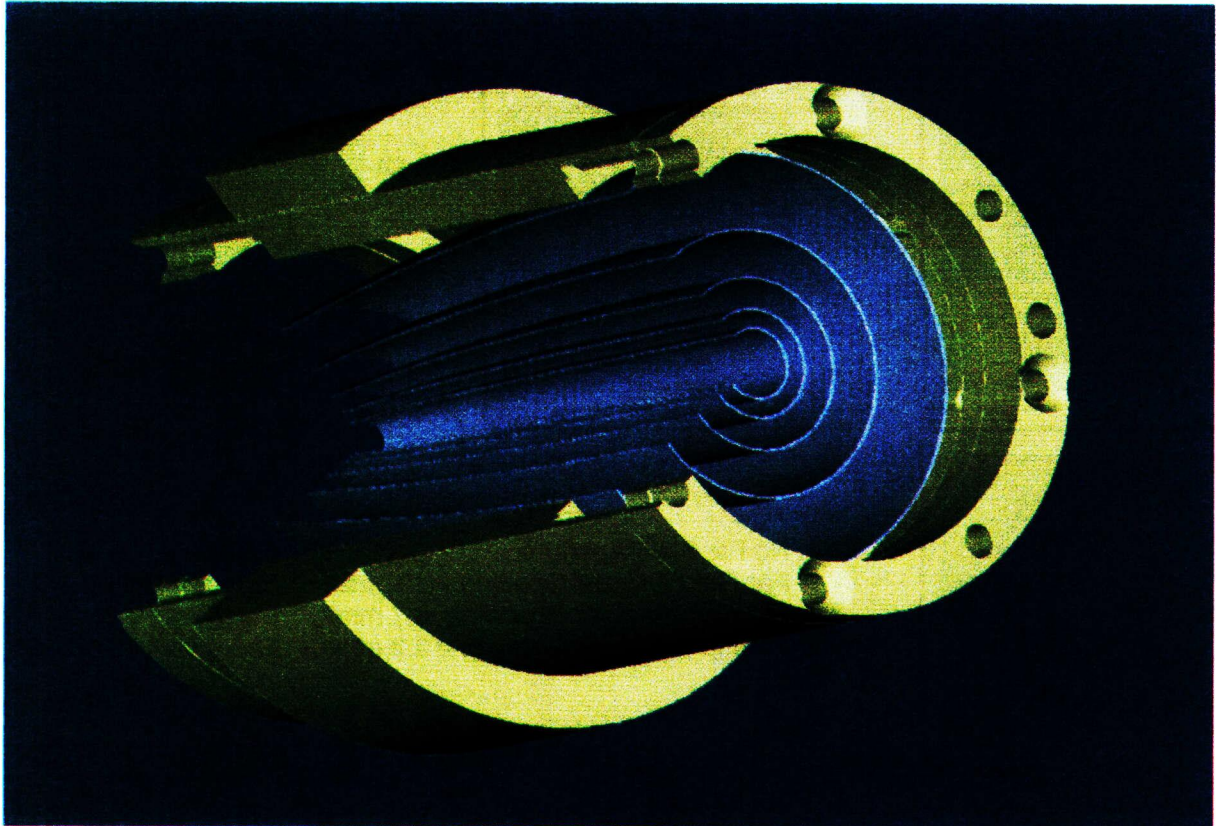


Fig 25. CAD rendering of first prototype grazing incidence collector.